Carbon 175 (2021) 490–498

Contents lists available at ScienceDirect

Carbon

journal homepage: www.elsevier.com/locate/carbon

Research Article

# Quantum transport in functionalized epitaxial graphene without electrostatic gating

E.H. Lock [a, *], J.C. Prestigiacomo [a], P. Dev [c], A. Nath [d], R.L. Myers-Ward [b], T.L. Reinecke [b], D.K. Gaskill [b], M.S. Osofsky [a]

[a] Materials Science and Technology Division, U. S. Naval Research Laboratory, Washington, DC, 20375, USA
[b] Electronics Science and Technology Division, U. S. Naval Research Laboratory, Washington, DC, 20375, USA
[c] Department of Physics and Astronomy, Howard University, Washington, DC, 20059, USA
[d] Postdoctoral Associate from George Mason University in Residence at the US Naval Research Laboratory, Washington, DC, 20375, USA

ARTICLE INFO

*Article history:*
Received 19 May 2020
Received in revised form
20 September 2020
Accepted 25 September 2020
Available online 29 September 2020

ABSTRACT

Graphene, the first isolated two-dimensional material, has captivated researchers for the last decade due to its unique structure that leads to novel electronic, chemical, mechanical, and thermal properties. The most intriguing properties are the large electronic mobilities that are achievable for low carrier concentrations and the large tunability of graphene's electrical properties via electrostatic gating, in which the Fermi energy is shifted relative to the charge neutrality, or Dirac, point and the high electronic mobilities obtained when the Fermi energy is close to that point. In this report, we show that both covalent and non-covalent functionalization of graphene leads to adsorbate-induced doping. This results in a three-fold increase in the graphene systems' mobilities and the observation of quantum transport phenomena (Hall effect plateaus, Shubnikov-de Haas oscillations, and Berry's phase) which were not observed in the unfunctionalized graphene. This ability to control the electronic properties without electrostatic gating is critical for chemical and biological sensing, optical, and electronic applications, which require both low carrier concentrations and the attachment of nanocrystals, biomolecules, increased adhesion and wettability of graphene layers, and enable strong cohesion between graphene layers in stacked graphene structures.

Published by Elsevier Ltd.

The quest to engineer graphene's electronic and chemical properties, graphene functionalization, i.e., utilizing specific reactions and doping species (atoms, ions, organic molecules, nanocrystals, self-assembled monolayers, polymers), has been the topic of intense research [1–5]. Pristine graphene is inert which is a major limitation for applications. The attachment of atoms and organic molecules to graphene is a challenge because the conversion of $sp^2$ to $sp^3$ bonding introduces defects in the crystal structure [2], leading to the degradation of its electrical properties through localization and/or the shifting of the Fermi energy, $E_F$, away from the charge neutrality point, increasing the carrier concentration, thus reducing the mobility [6,7]. Indeed, numerous organic molecules have been used for covalent and non-covalent functionalization of graphene [4,8–10] to enable the application of graphene hybrid materials in biosensing, photodetection, organic emitting diodes, supercapacitors, catalytic and biomedical applications [6,11–13]. Depending on the type of organic molecule and bonding structure, graphene's mobility can be modulated from 1 to 8900 $cm^2V^{-1}s^{-1}$ [13].

This work demonstrates covalent and non-covalent functionalization-induced (adsorbate) doping of graphene, which resulted in increased mobility compared to unfunctionalized graphene films. Furthermore, these phenomena manifest as signatures of the quantum Hall effect (QHE), a series of plateaus of the Hall resistivity, $R_{xy}$, which occurs *exclusively* in high-mobility, two-dimensional electronic systems [14–18]. These plateaus are accompanied by Shubnikov-de Haas (SdH) oscillations [18,19] in the longitudinal magnetoresistance, which occur as $R_{xy}$ reaches fractions of the quantum resistance (i.e., $R_{xy} = h/(\nu e^2)$, where the filling factor $\nu$ can be an integer or fraction, $e$ is the electron charge,

* Corresponding author.
*E-mail address:* evgeniya.lock@nrl.navy.mil (E.H. Lock).

https://doi.org/10.1016/j.carbon.2020.09.077
0008-6223/Published by Elsevier Ltd.

and $h$ is Planck's constant) and result from carriers at the Fermi surface circulating in cyclotron orbits with energy levels that are quantized (Landau levels). The unique structure of graphene causes the carrier wave functions to acquire a phase difference during the orbits called Berry's phase [12–14]. The observation of a quasi-QHE in low fields is significant because it only occurs in systems with high mobility, and provides a direct measurement of the quantum resistance, $h/e^2$.

While others have demonstrated surface transfer doping via functionalization and substitutional doping [19–26], there are only a few reports of the QHE in modified epitaxial graphene via surface [27,28] or electrostatic doping [29–32]. In this report, we demonstrate the ability to tune the Fermi level energy, and thus the carrier concentration, of epitaxial graphene by chemical functionalization leading to the observation of quantum transport phenomena, including the Berry's phase, in ungated epitaxial graphene, indicating that the functionalized graphene maintains the unique electronic character of pristine graphene. Our approach uses sparsely distributed chemical molecules for chemical functionalization, thus rendering the graphene surface reactive and amenable for further attachment of nanocrystals and biomolecules for applications.

Samples were grown on 8 × 8 $mm^2$ semi-insulating (SI), Si-face, on-axis, (0001) 6H–SiC coupons by chemical vapor deposition at 1570 °C under Ar ambient using an Aixtron VP508 reactor. We hypothesized that non-covalent (pyrene- and pyridine-based) and covalent (azide-based) molecules would compensate the substrate-induced charging of the epitaxial graphene, so several were used for the study. The non-covalent functionalization was performed using 1-hydroxypyrene (Pyr-OH) and 4-aminomethyl pyridine (Pyr-$NH_2$), while for covalent functionalization, 1-pyrenecarboxylic acid (Pyr-COOH) and N-ethylamino-4-azido-tertafluorobenzoate (TFPA-$NH_2$) were employed (Fig. 1). Covalent functionalization with TFPA-$NH_2$ was shown previously [33,34].

Comprehensive analyses of the chemical and structural properties of the functionalized epitaxial graphene were conducted using X-ray photoelectron spectroscopy (XPS), Raman spectroscopy, and microscopy (Figs. S1–S5, Tables S1–S3). The results indicate that functionalization changes the chemical composition and structure of the graphene layer inducing the chemical doping of the graphene [35]. The amount of chemical modification, type of molecule attachment (covalent vs. van der Waals), and attachment density depended on the molecule type. These chemical modifications led to surface doping via charge transfer between the graphene and the molecules attached to the surface, which, in turn, modified the graphene's transport properties, which were obtained using a Quantum Design Physical Property Measurement System (PPMS). Density functional theory (DFT) was employed to evaluate the bond strengths and charge transfer between the molecules and the graphene layer.

## 1. Transport properties

Fig. 2 shows the temperature-dependent sheet resistance, charge-carrier density, and carrier mobility measurements obtained using the van der Pauw configuration of as-received and functionalized epitaxial graphene. The data were obtained from measurements over 8 × 8 $mm^2$ samples and an average over many terraces and steps. Remarkably, the $n$-type, metallic transport properties exhibited by the as-grown graphene films were maintained for all functionalized ones. The carrier density ($n_{Hall}$) was almost temperature independent for both the as-grown and functionalized graphene. However, $n_{Hall}$ was reduced by nearly an order of magnitude for the functionalized graphene (Pyr-OH, Pyr-COOH, and Pyr-$NH_2$). The carrier mobility ($\mu_{Hall}$) generally increased as the temperature decreased in all cases with the magnitude dependent on the functionalization type. However, mild disorder-induced weak localization effects, evident as small increases in resistivity and decreases in the Hall mobility at low T and a zero-field peak in the magnetoresistance, were observed in all samples, including the pristine epitaxial graphene. While the mobility of as-grown graphene increased to 1000 $cm^2\ V^{-1}s^{-1}$ at 4 K, the $\mu_{Hall}$ of the functionalized films increased three-fold to 2700–3000 $cm^2\ V^{-1}s^{-1}$ at 4 K. In general, we observed an overall improvement of the electronic properties over plasma functionalization (Figs. S6 and S7). A Hall bar, fabricated over a single SiC terrace (Fig. S8) and functionalized with TFPA-$NH_2$, exhibited similar properties. The sheet resistance of the TFPA-$NH_2$ functionalized graphene was very similar to the as–grown sample at low temperatures. At the same time, $n_{Hall}$ was reduced by a factor of 2.5, and $\mu_{Hall}$ increased two-fold to approximately 2000 $cm^2\ V^{-1}s^{-1}$at 4 K. A comparison of our carrier mobility versus carrier density data (Fig. 3) with that of top-gated epitaxial graphene at 5 K and 300 K obtained from the literature [23] (references given in the caption) verifies that tuning the carrier concentration and mobility using our functionalization approach is equivalent to that of electrostatic gating.

Further verification that the mobility increased in the functionalized graphene was obtained by observing signatures of the QHE. The QHE plateaus in monolayer (ML) and bilayer (BL) graphene can be distinguished by their Landau level (LL) indexes of $\nu = 4\,(n_{ML} + ½)$ and $\nu = 4n_{BL}$, respectively, where $n_{ML} = 0, 1, 2, \ldots$ and $n_{BL} = 1, 2, 3, \ldots$ A lower LL index means $E_F$ is closer to the CNP. Fig. 4(a–e) display $R_{xy}$ versus $B$ for the pristine (as-received) and functionalized graphene. As expected, no identifiable plateaus appear in the as-received graphene, due to the excessive intrinsic doping of the graphene layer via charge transfer from the underlying SiC substrate [37]; however, several appear in the functionalized samples. In addition, apparent SdH oscillations are observed in the $R_{xx}$ versus $B$ data in Fig. 4(f and g). The specific LLs and the magnetic field magnitude at which the plateaus are observed vary among the functionalization types. Plateaus (arrows in Fig. 4 g and

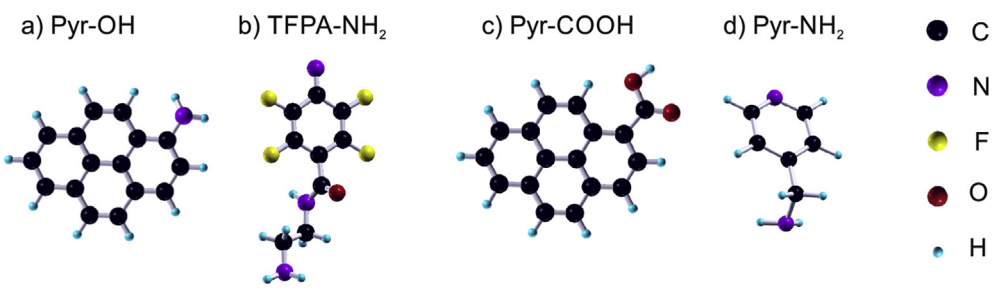


**Fig. 1.** Molecular adsorbates used for epitaxial graphene functionalization. (A colour version of this figure can be viewed online.)

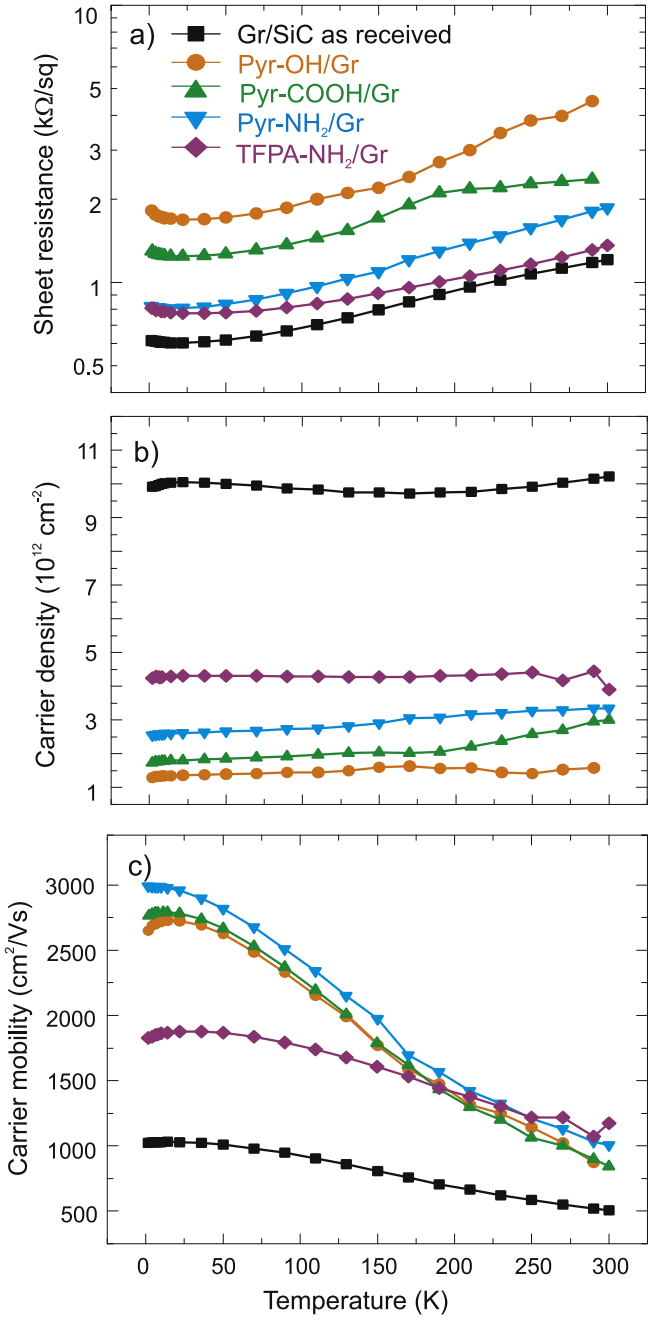


**Fig. 2.** Sheet resistance (a), carrier density (b), and carrier mobility (c) variation as a function of temperature for as-received and chemically functionalized epitaxial graphene on SiC. (A colour version of this figure can be viewed online.)

j) observed at filling factors not associated with either monolayer or bilayer graphene were also seen in the ($8 \times 8$ mm$^2$) functionalized samples, possibly because the measurements encompass many SiC terraces and steps where both monolayers and bilayers are present, which can lead to a distortion of the QHE [38,39]. Another possibility is the presence of a background conduction channel composed of low mobility carriers that do not participate in the QHE [40,41]. Such a channel could arise from non-uniform coverage of functionalization molecules and/or charge donation from gas adsorbates on the graphene surface leading to an $E_F$ distribution. Therefore, we assumed that the leading contribution is from monolayer graphene and attempted to assign the plateaus to the closest allowable monolayer graphene LL indices.

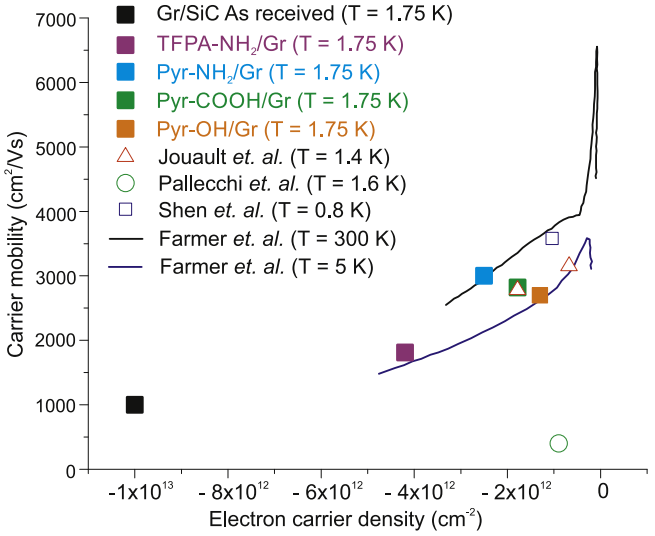


**Fig. 3.** Comparison of electronic properties of low-field Hall data between chemically-functionalized and electrostatically gated epitaxial graphene. Carrier mobility and electron carrier density data are taken from the works of Jouault et al. [29], Pallecchi et al. [28], Shen et al. [30], and Farmer et al. [36]. (A colour version of this figure can be viewed online.)

The oscillatory component of the longitudinal magnetoresistance in graphene can be described by the semi-classical equation $\Delta R_{xx} = R(B, T)\cos[2\pi(B_F/B + ½ + \beta)]$, where $R(B, T)$, $B_F$, and $2\pi\beta$ are the SdH amplitude, frequency, and Berry's phase, respectively. By constructing a fan diagram (plotting the LL index $n$ ($n$+½) associated with each SdH minima (maxima) versus its location in $1/B$), a linear relationship is formed, allowing the extraction of Berry's phase and the SdH frequency from the $y$-intercept and slope, respectively. Such a diagram is shown in Fig. 5 for each functionalization type revealing a Berry's phase close to $\pi$, which is consistent with the existence of Dirac quasiparticles in graphene demonstrating that the samples still have graphene's distinctive band structure and hence that the functionalization did not change the graphene structure or the underlying buffer layer.

The SdH oscillation frequency can be used to calculate the sheet carrier density localized into a quantum Hall state using $n_{SdH} = 4B_F/\phi_0$, where $\phi_0$ is the flux quantum, yielding values of the order of $10^{12}$ cm$^{-2}$ for all functionalization types with a trend of decreasing $n_{SdH}$ as one moves from TFPA-NH$_2$, Pyr-NH$_2$, Pyr-COOH, to Pyr-OH and a ratio of $n_{SdH}/n_{Hall}$ ~87.4%, 90%, 86.7%, and 73.2%, respectively. This suggests that a relatively large background conduction channel is indeed responsible for the large degree of imperfect filling factor quantization for the Pyr-OH functionalized sample. Regardless, a majority fraction of carriers for each functionalization type participate in the charge carrier quantization. Thus the arrangement of carrier density values from highest to lowest remains the same for the two calculation methods.

Generally, the mobility of quantized carriers, independent of additional transport channels, can be obtained from the Lifshitz-Kosevich theory for the temperature dependence of the SdH oscillation amplitude,

$$\Delta R_{xx}(T, B) \propto \frac{\alpha T/\Delta E_N(B)}{\sinh[\alpha T/\Delta E_N(B)]} e^{-\alpha T_D/\Delta E_N(B)},$$

where $\alpha = 2\pi^2 k_B$, $\Delta E_N(B) = heB/2\pi m^*$ is the energy spacing between adjacent LLs, $B$ is the field position of the N$^{th}$ minimum in $R_{xx}$, $m^*$ is the effective mass of the charge carriers, $T_D = h/4\pi\tau k_B$ is

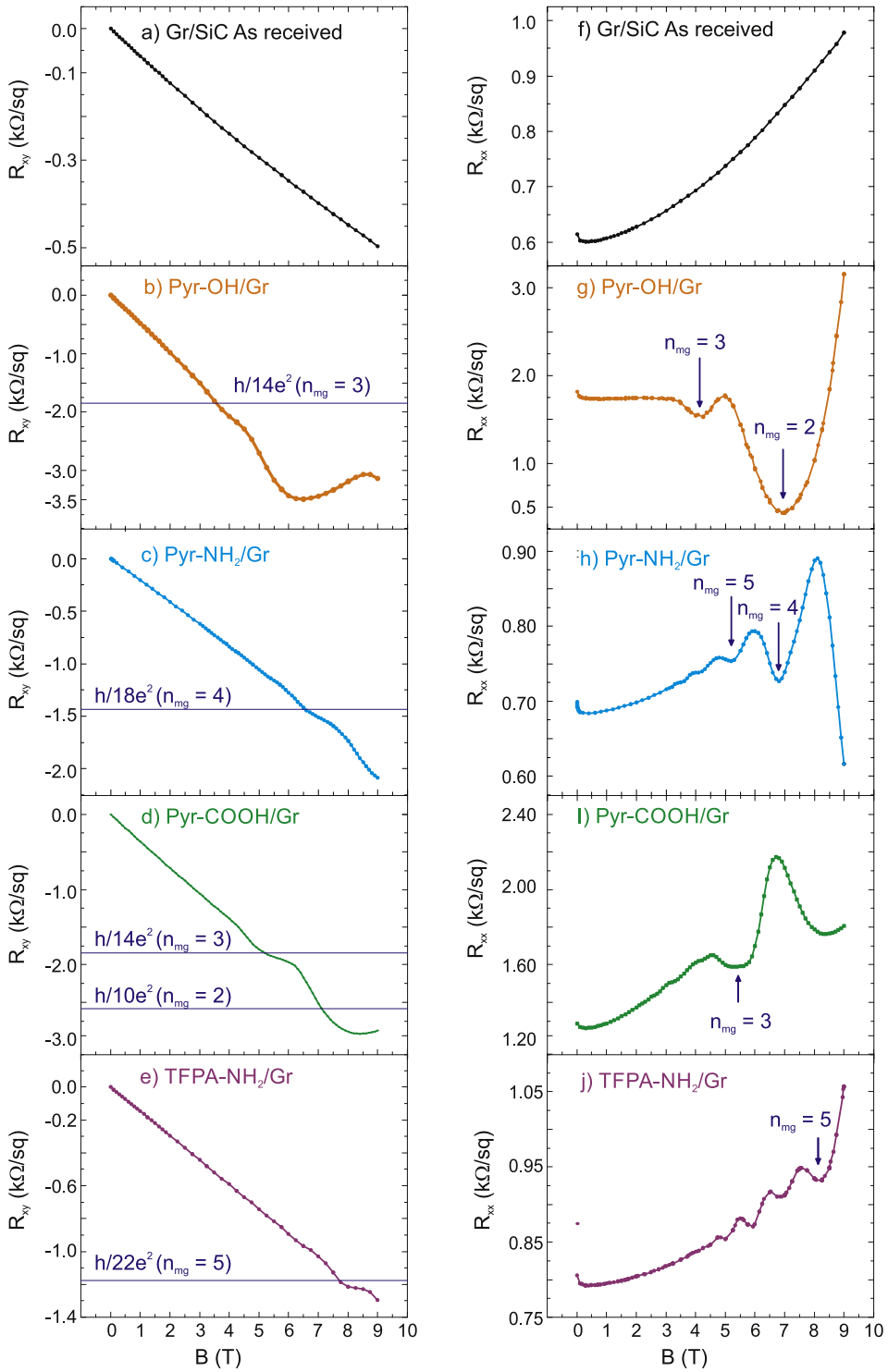


**Fig. 4.** Hall effect plateaus (a–e) and Shubnikov de Haas oscillations (f–j) of functionalized epitaxial graphene at T = 1.75 K. (A colour version of this figure can be viewed online.)

the Dingle temperature, and $\tau$ is the quantum lifetime due to carrier scattering. An analysis of the temperature dependence of the SdH oscillations was performed on the TFPA-$NH_2$ functionalized Hall bar sample and is shown in Fig. 6. The oscillation amplitudes at different temperatures for a given LL field value, normalized by the $T = 2$ K amplitude ($\Delta R_{2K}$), were plotted as a function of temperature and then fit to the function $\frac{\alpha T/\Delta E_N(B)}{\sinh[\alpha T/\Delta E_N(B)]}$, which yielded $m^* = (0.037 \pm 0.001)m_0$, where $m_0$ is the free electron mass. This value is consistent with those reported for exfoliated graphene flakes [42]. The slope of a linear fit to the quantity $\ln\left(\Delta R_{xx} B \sinh\left[\frac{\alpha T}{\Delta E_N(B)}\right]\right)$ for several fields at constant $T = 2$ K plotted as a function of $1/B$ yielded $T_D \sim 31$ K and a carrier lifetime $\tau \sim 3.9\text{x}10^{-14}$ s, which is about ten times shorter than that of exfoliated graphene. Consequently, the mobility of quantized charges in the TFPA-$NH_2$ functionalized samples is $\mu_{SdH} \sim 1800$ $cm^2V^{-1}s^{-1}$, which is close to the exact value

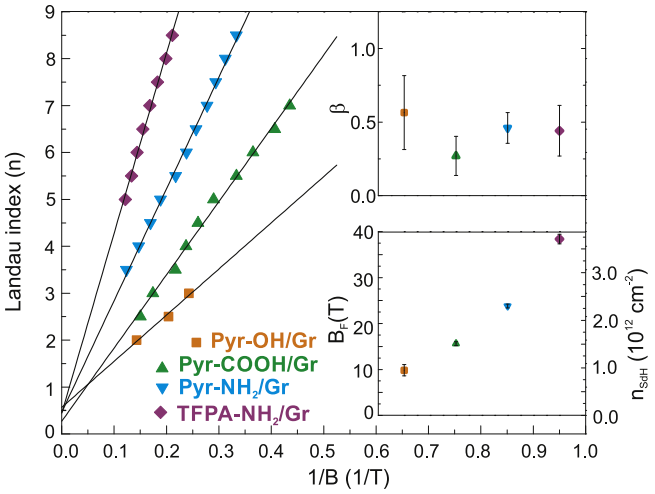


**Fig. 5.** A fan diagram for SdH oscillations at $T = 1.75$ K for different functionalization types. The solid lines are linear fits the data, which extrapolate to a $y$-intercept value (upper inset) that corresponds to Berry's phase ($2\pi\beta$) for each functionalization type. The lower inset displays the slope of the linear fit ($B_F$) on the left $y$-axis corresponding to the SdH oscillation frequency, and the sheet carrier density derived from $B_F$ on the right $y$-axis. Different functionalization types are color coded in the inset plot (no $x$-axes of the inset plots are included). (A colour version of this figure can be viewed online.)

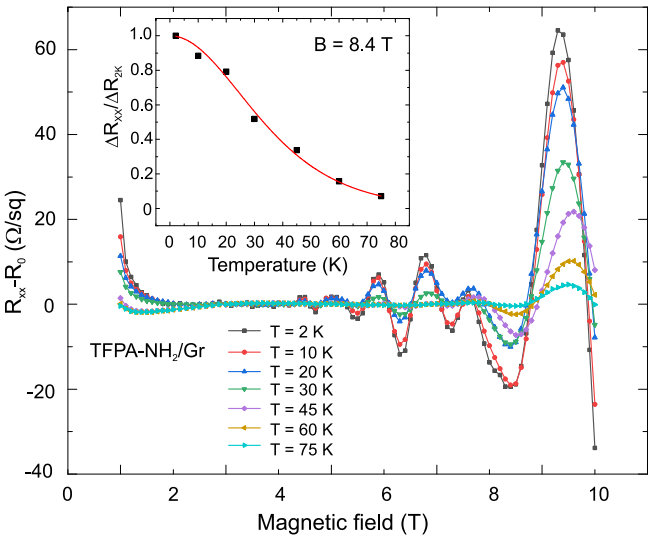


**Fig. 6.** The longitudinal magnetoresistance of the TFPA-$NH_2$ sample after subtraction of background ($R_0$) fit the data using a 3rd order polynomial function in the field range 1.5 T–6.5 T. The upturn at the low field is due to weak localization. Inset: The amplitude of the MR peak at 8.4 T normalized by the 2 K value. The solid line is a fit to the Lifshitz-Kosevich formula. (A colour version of this figure can be viewed online.)

determined by the ordinary Hall effect.

Density functional theory calculations were performed to determine how the functionalization changes the density of states near CNP and establish the nature of bonding (covalent vs. non-covalent) between molecules and graphene.

## 2. Density functional theory (DFT) calculations

Density Functional Theory (DFT) calculations were performed using the Quantum-ESPRESSO package [43]. The generalized gradient approximation [44] of the Perdew-Burke-Ernzerhof (PBE) functional [45] was used to account for the exchange-correlation effects. Van der Waals interactions between non-covalently bonded molecules and graphene, and dispersion correction terms (DFT-D) [46,47] were included in the calculations to understand the structural properties of the composite structures, in turn shedding light on the mechanisms that are responsible for the carrier modulation caused by functionalization. In the experiment, the molecules were adsorbed on graphene grown on SiC, ($n$-doped graphene with $n \sim 10^{13}$ cm$^{-2}$). To emulate these effects without explicitly including SiC, DFT calculations were performed for the molecule-graphene composite structures that were $n$-doped. For comparison, we have provided the results for neutral graphene as well (Fig. S9). We found that the results for the structural properties are similar in the case of neutral and $n$-doped graphene (Fig. S9). It should be pointed out that several effects, such as the presence of defects and inhomogeneous coverage of the adsorbates, might affect the graphene-molecule binding density. However, due to the size of the structures involved in these calculations, we studied the interactions between pristine graphene and different adsorbates for one concentration of the molecules only (1 adsorbate per 72 carbons). Nevertheless, the DFT results are instructive and help to understand the local bonding of the adsorbate to the graphene sheet.

Fig. 7 shows molecular geometries of equilibrium structures obtained by relaxing the forces on the constituent atoms with the relaxation threshold set to be better than $10^{-4}$ Ry/a. u. The nature of the bonding was not assumed *a priori* but was obtained via structure optimization. Our DFT calculations show that the four molecules bind differently to the graphene matrix, with the bond lengths being indicative of the strength of the bonds formed between the molecules and graphene (summarized in Table within Fig. S9). The Pyr-OH molecule forms the weakest bond with graphene, with the physisorbed molecule situated at a distance of ~3.31 Å from the $n$-doped graphene sheet (Fig. 7b). This weak van der Waals interaction between the two sub-systems means that the graphene remains planar and retains its electronic structure upon the adsorption of the Pyr-OH molecule.

On the other hand, the TFPA-$NH_2$ molecule forms the strongest bond with graphene (distance ~ 1.48 Å) due to strong bidentate carbene covalent bonding with graphene (Fig. 7c). This strong attachment results from $sp^3$-rehybridization of the graphene locally, with the graphene carbons participating in the bond. In the relaxed structure, the TFPA-$NH_2$ molecule is canted relative to the surface, with the benzene ring tilted towards the graphene sheet. It is expected that the fluorine terminated benzene rings in the TFPA-$NH_2$ molecule would result in considerable steric hindrance, resulting in a sparse molecular distribution.

The bond-strengths for the cases of Pyr-COOH and Pyr-$NH_2$ functionalizations are between the two extreme cases of Pyr-OH and TFPA-$NH_2$. Surprisingly, the −OH & −COOH functional groups attached to the same four benzene rings structure result in substantially different bonds between the molecules and graphene. Unlike the case of the Pyr-OH molecule (Fig. 7b), the Pyr-COOH molecule is chemisorbed due to the formation of a weak covalent bond between the carbons of pyrene and graphene (bond length of 1.63 Å) that results in a local $sp^2$ to $sp^3$ rehybridization of the graphene (Fig. 7d). The bond between the graphene and the Pyr-COOH molecule is weaker than the C–C $sp^3$ bond length of ~1.54 Å. The resultant partial $sp^2$-$sp^3$-character of graphene upon adsorption of Pyr-COOH is expected to change graphene properties to a lesser degree than the TFPA-$NH_2$ adsorption. This can be inferred from the degree of $sp^3$-rehybridization, with bonded carbon atoms of graphene raised by ~0.22 Å from their original position for Pyr-COOH adsorption, compared to 0.53 Å in the case of TFPA-$NH_2$ adsorption. This smaller distortion would mean that the molecule

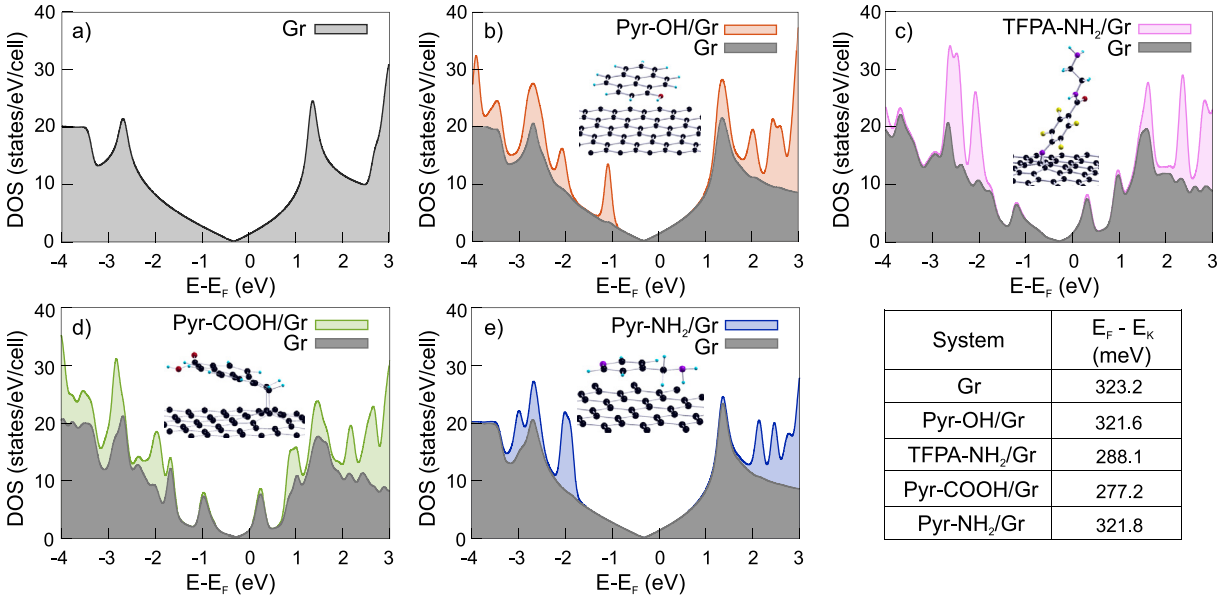


| System | $E_F$ - $E_K$ (meV) |
|---|---|
| Gr | 323.2 |
| Pyr-OH/Gr | 321.6 |
| TFPA-$NH_2$/Gr | 288.1 |
| Pyr-COOH/Gr | 277.2 |
| Pyr-$NH_2$/Gr | 321.8 |

**Fig. 7.** First-principles calculation results: Total density of states (TDOS) of (a) *n*-doped freestanding graphene, (b–e) molecule-graphene complexes, along with the contributions of graphene in each complex to the respective TDOS, and equilibrium geometries of the molecule-graphene complexes. The Fermi level ($E_F$) is used as reference energy, and X/Gr is an abbreviation for "molecule X on graphene." The table gives the energy difference between the Fermi level and the minimum of DOS (identified as energy, $E_K$, corresponding to the Dirac-point). The molecular geometries in Fig. 7b-e are the equilibrium structures obtained by relaxing the forces on the constituent atoms with the relaxation threshold set to be better than $10^{-4}$ Ry/a. u. (A colour version of this figure can be viewed online.)

adsorption would not appreciably affect graphene properties within the Pyr–COOH–graphene complex, as also seen in the experiment. The Pyr-$NH_2$ molecule forms a non-covalent bond with graphene with a bond length of ~2.63 Å (Fig. 7e), with graphene retaining its properties.

The structural differences in the molecule-graphene complexes, in turn, dictate the electronic structure properties of the complexes, with the adsorbed molecules affecting graphene properties to different extents. This can be seen in the density of state (DOS) plots in Fig. 7b–e, which show the total density of states (TDOS) of the complexes, along with the contribution of graphene to the TDOS in each complex. The latter is obtained by projecting DOS onto graphene and can be compared with the DOS of freestanding graphene that has been *n*-doped (Fig. 7a). In the case of composite structures that are primarily bonded via van der Waal's interactions (Pyr-OH and Pyr-$NH_2$), the DOS projected onto graphene (Fig. 7b, e) shows the preservation of graphene's electronic structural properties, with an identifiable Dirac-point at the minimum of the projected DOS (cf. Fig. 7a). On the other hand, TFPA-$NH_2$ and Pyr-COOH form covalent bonds with graphene, resulting in local rehybridization of bonds within the graphene matrix. The effects of rehybridization are visible in Fig. 7c and 7d, where the DOS projected onto the graphene shows considerable changes around the Dirac-point (at the minimum of DOS projected onto graphene). The Table in Fig. 7 gives the shifts in the Fermi level relative to the Dirac-point in *n*-doped pristine graphene and the graphene-molecule complexes. In all cases, the adsorbed molecules accept electrons from graphene (*p*-doping it in the process) to some extent, which shifts the Fermi level closer to the Dirac-point (cf. value for *n*-doped freestanding graphene in the Table). Significant changes in $E_F$-$E_k$ (CNP) values of 46 meV and 35 meV were detected in covalently functionalized graphene with the Pyr-COOH and the TFPA-$NH_2$ molecules compared to pristine graphene, respectively, which is comparable to electrostatically gated graphene [24]. Note that when we have neutral graphene, TFPA-$NH_2$ *n*-dopes graphene to a greater extent than the Pyr-COOH. However, when we include the effect of the substrate by the *n*-doping of the graphene, the order reverses because TFPA-$NH_2$ is less electronegative than Pyr-COOH, so when the former is adsorbed on *n*-doped graphene, it accepts electrons less readily. This is in qualitative agreement with the experiment.

## 3. Discussion

These results demonstrate that the chemical doping of epitaxial graphene can be achieved via functionalization with several covalent and non-covalent molecules. All of the functionalized epitaxial graphene studied exhibited quantum transport phenomena, both quasi-QHE, and SdH oscillations, that was not observed in as-grown, unfunctionalized samples. Most significantly, a careful analysis of the SdH oscillations revealed the presence of Berry's phase that is consistent with that of pristine graphene flakes suggesting that the functionalization did not significantly alter the structure of the epitaxial graphene. Experimental and theoretical analyses indicated that these results are due to the fact that the major effect of the chemical doping is the shift of $E_F$ towards the Dirac point. Indeed, our transport experiments show that the mobility of the graphene/functional molecule complexes from the highest to lowest at low temperature changes in the following order Pyr-$NH_2$ > Pyr-COOH ~ Pyr-OH > TFPA-$NH_2$. As mentioned above, the carrier density at the same conditions from the highest to lowest vary as follows TFPA-$NH_2$ > Pyr-$NH_2$ > Pyr-COOH > Pyr-OH. Thus, the covalent functionalization results in the most significant modification in electronic properties (increase in density, decrease in mobility). From the non-covalent functionalization, Pyr-$NH_2$ has the strongest effect on graphene electronic properties, while Pyr-OH has the least. In all cases, the non-covalent functionalization perturbs less than the electronic properties compared to the covalent functionalization. This is due to the differences in their attachment (bond strength) and *p*-doping effects of the graphene films. Based on the DFT calculations, the bond strength (from strongest to weakest) vary in the following order TFPA-$NH_2$ > Pyr-COOH > Pyr-$NH_2$ > Pyr-OH. The *p*-doping magnitude changes from

strongest to weakest in the following order Pyr-COOH > TFPA-$NH_2$ > Pyr−$NH_2$ > Pyr−OH for *n*-doped graphene and TFPA-$NH_2$> Pyr-COOH > Pyr-$NH_2$> Pyr-OH for neutral graphene, suggesting the strongest bond formation between the TFPA-$NH_2$ molecule and the weakest between Pyr-OH. The agreement between experiment and theory is reasonable. One of the main differences are in the effect of Pyr-$NH_2$ compared to Pyr-COOH and Pyr-OH on the graphene films. MicroRaman analysis (Table S3, Figs. S2–S5) show that while Pyr-$NH_2$ and TFPA-$NH_2$ have no attachment site preference (both steps and terraces are uniformly functionalized), the Pyr-COOH and the Pyr-OH prefer terrace sites compared to steps. This is most likely due to their large benzene ring structure which may induce steric hindrance effects preventing attachment to steps. Thus, the first key reason for the discrepancy of experiment and theory is the nature of molecular deposition. The latter vary depending on its molecular structure - Pyr-$NH_2$ is a very small molecule, so it is easy to have higher coverage per unit area, TFPA-$NH_2$ is much larger molecule and it is tilted toward the graphene surface, so the relative coverage per unit area is smaller. The pyrene-based molecules with large number of benzene rings functionalize the terraces preferentially, thus they may have much smaller coverage per unit area compared to the other adsorbates. In addition, the nature of the epitaxial graphene and the non-uniformity of the SiC substrate is difficult to integrate in the DFT calculations - while single layer graphene is grown on the terraces, 2–3 layers are present on the steps of the SiC substrate. Thus, the DFT calculations should be used as a guide to the obtained experimental results. Nevertheless, our results show that the proper selection of the organic molecule is the key for graphene modification as it changes the amount of induced charge (doping) of the graphene film. Furthermore, molecules with a similar chemical composition (the same number of benzene rings and different functional groups, e.g., hydroxyl vs. carboxyl) can cause a different level of chemical doping. Lastly, sparse functionalization of graphene with organic chemical moieties induces a substantial effect in graphene's density of states (e.g., electronic structure) and enables modification of electronic properties on demand.

This discovery is a key technological step toward the development of graphene-based technologies since the functional groups can be used as anchors for the attachment of 0D materials (quantum dots, metal, and metal oxide nanoparticles), biomolecules (peptides, DNA, antibodies, aptamers), fluorescent dyes and other organic and metal-organic complexes leading to increase in the selectivity, sensitivity, and robustness of graphene-based hybrid electrochemical, colorimetric, fluorescent, photoluminescent, chemiresistive, magnetic and field-effect sensors. This functionalization approach impacts the sensor domain in a wide range of subdisciplines, including the detection of harmful gas molecules, volatile organic compounds, chemical warfare agents, heavy ions, pathogens, and other biological threats. Additionally, this approach may also impact the fields of energy generation (solar cells) and storage, photodetection, and RF electronics (RF field-effect transistors, mixers, and future device functionalities). Lastly, we note that our graphene functionalization scheme enables the production of two-dimensional material heterostructures because the selective functionalization leads to cohesive bonding between different 2D layers and can influence the modulation of heterostructure properties the modification of interlayer spacing thus providing intriguing opportunities for the demonstration of new quantum effects.

In summary, we have shown that the proper selection of organic molecules is the key to graphene's chemical modification. It changes the amount of induced charge (i.e., doping) of epitaxial graphene films. Indeed, as expected with reduced carrier density, the mobility of the functionalized graphene increased by a factor of two to three compared to the pristine graphene at low temperatures. This was due to the induced *p*-doping effect that compensates the natural *n*-type doping known to be present in single-layer graphene and shifts the Fermi energy. Furthermore, pyrene molecules with a similar chemical composition (the same number of benzene rings and different functional groups: hydroxyl vs. carboxyl) had different bonding strengths and different doping levels. As a result of the increased mobility, Hall effect plateaus, Berry phase, and Shubnikov de Haas oscillations were observed without electrostatic gating. Surprisingly, these quantum phenomena were detected not only in non-covalently bound pyrene- and pyridine-based molecules but also in covalently attached azide-based molecules. Our DFT calculations indicated that is due to the nature of the covalent and non-covalent bonds formed, which could not be assumed *a priori*. Unlike other functionalization approaches, our functionalized graphene films have active carboxyl, hydroxyls, and amine functionalities, which can be further utilized as (1) linkers for nanocrystals (metal oxides, metals, quantum dots) and biomolecules which can be used for improving the current state of the art of graphene sensors, transistors, photodetectors, energy storage devices, and (2) it may lead to the observation of novel quantum phenomena if implemented in two dimensional heterostructures for the production of novel hybrid systems with enhanced layer cohesion.

## 4. Materials and methods

### 4.1. Graphene growth

Epitaxially grown graphene on silicon carbide (SiC) was achieved via Si sublimation from semi-insulating (SI), Si-face, on-axis, (0001) 6H−SiC coupons using an Aixtron VP508 chemical vapor deposition reactor. The growth was done at 1570 °C and 100 mbar using Ar ambient. The Ar is used to suppress the sublimation of Si to control the thickness of the epitaxial graphene layers. Before growth, the substrates were in-situ $H_2$ etched to prepare the SiC surface for epitaxial graphene growth. The surface was prepared by forming a bilayer stepped morphology and removing any polishing scratches created during the manufacturing of the SiC substrate. Samples were cooled in Ar to 800 °C, and the reaction tube was evacuated. The average thickness of the epitaxial graphene was ~1.5 monolayers measured by X-ray photoelectron spectroscopy (XPS). Additional details can be found in Ref. [48].

### 4.2. Graphene functionalization

A 1-hydroxypyrene solution was used as received. The 1-pyrenecarboxylic acid was dissolved in methanol to make a 20 mM solution. The graphene chips were incubated for 1 h in both solutions. The graphene chip was incubated at 190 °C for 6 h for 4-aminomethyl pyridine. The covalent functionalization is based on forming a carbon bond between the azide-containing molecules and the graphene using N-ethylamino-4-azidotetrafluorobenzoate (TFPA-$NH_2$). The 4 ml solutions of both compounds were prepared in methanol. Then, the graphene chips were placed in solutions and exposed to UV light for 10 min. Both functionalization types are tunable by adjusting the solution molarity and incubation times. After functionalization, the graphene chips were rinsed with methanol and isopropyl alcohol and dried with nitrogen.

The chemical composition of pristine and functional graphene surfaces was analyzed by X-ray photoelectron spectroscopy (Thermo Fisher). The structural analysis (point analysis and micro Raman maps) was performed using a Thermo Scientific DXRxi Raman confocal imaging system using a 532 nm probe having 9.6 mW incident power and spot diameter of about 0.7 μm. The

electronic transport measurements were performed in a Quantum Design Physical Properties Measurement System. The temperatures were varied between 1.75 and 400 K in applied magnetic fields between ±9 T. To obtain accurate sheet resistance values, the square samples' four corners were wired in a van der Pauw configuration by bonding 1-mil Au leads with Ag paint. The excitation currents used for these experiments were typically ~ 1 μA DC.

### 4.3. Calculation details

Graphene's electronic-structure properties are changed by molecules adsorbing to it. Density Functional Theory (DFT)-based calculations were used to study these property changes. In the theoretical work, a subset of molecules was chosen from the experiments with 1-hydroxypyrene (Pyr-OH) and TFPA-$NH_2$ to explore the non-covalent and covalent functionalization of graphene, respectively. These calculations were performed using the Quantum-ESPRESSO package [43]. The generalized gradient approximation [44] of Perdew-Burke-Ernzerhof (PBE) [45] was used to account for the exchange-correlation effects. To account for van der Waals interactions between non-covalently bonded molecules and graphene, dispersion correction terms (DFT-D) [46,47] were included in the calculations. A 6 × 6 × 1 supercell (72 atoms) of graphene and a vacuum layer of about 30 Å thick normal to the graphene surface were used. This vacuum layer provided ample space above the graphene for the chemical to be functionalized while maintaining sufficient isolation from the images of the composite structure.

A kinetic energy cutoff of 40 Ry for expanding the wave functions and a cut-off of 350 Ry for charge densities were used. The Monkhorst-Pack scheme [49] was used to generate the Γ-centered, 14 × 14 × 1 k-point grid. To obtain the nuclear positions used in this work, the structure was relaxed after the adsorption of the molecules onto the graphene, with the relaxation threshold set to be better than $10^{-4}$ Ry/a. u.

### 4.4. Graphene device fabrication and testing

A bi-layer process and low post photoresist dispersion bake temperature were employed to minimize graphene surface contamination [48]. The 120 × 10 μm Hall bars were etched into the graphene film using a 60 W oxygen plasma etch (Axic BENCHMARK 800-II) for 120s. The wire bonding pads were formed on etched SiC by depositing 10 nm Ti and 200 nm Au with e-beam evaporation. The graphene leads were exposed to a 5-min UV-ozone treatment prior to contact metal deposition to achieve low contact resistance. After each processing step, the samples were annealed at 400 °C for 30 min in $Ar/H_2$ gas environment to reduce contact resistance and to remove any contaminants [50,51].

## CRediT authorship contribution statement

**E.H. Lock:** Conceptualization, Investigation, Methodology, Data curation, Formal analysis, Visualization, Validation, Writing - review & editing. **J.C. Prestigiacomo:** Data curation, Formal analysis, Investigation, Visualization, Writing - review & editing. **P. Dev:** Software, Data curation, Investigation, Validation, Visualization, Writing - review & editing. **A. Nath:** Investigation, Data curation, Formal analysis. **R.L. Myers-Ward:** Data curation, Investigation, Visualization. **T.L. Reinecke:** Formal analysis, Writing - review & editing. **D.K. Gaskill:** Data curation, Investigation, Formal analysis, Visualization, Writing - review & editing. **M.S. Osofsky:** Formal analysis, Supervision, Writing - review & editing.

## Declaration of competing interest

The authors declare that they have no known competing financial interests or personal relationships that could have appeared to influence the work reported in this paper.

## Acknowledgments

This work was funded by the Office of Naval Research (ONR) through the US Naval Research Laboratory Basic Research Program.

This work used the computer resources were provided by the DoD High Performance Computing Modernization Program and the Extreme Science and Engineering Discovery Environment (XSEDE), which is supported by National Science Foundation grant number ACI-1548562 (Project: PHY180014). PD was funded by the National Science Foundation (NSF) through Grant No. DMR-1752840.

## Appendix A. Supplementary data

Supplementary data to this article can be found online at https://doi.org/10.1016/j.carbon.2020.09.077.

## References

[1] K.C. Kemp, Y. Cho, V. Chandra, K.S. Kim, Noncovalent Functionalization of Graphene, Functionalization of Graphene, 2014, pp. 199–217.
[2] A. Criado, M. Melchionna, S. Marchesan, M. Prato, The covalent functionalization of graphene on substrates, Angew. Chem. Int. Ed. 54 (2015) 10734–10750.
[3] C. Chua, M. Pumera, Covalent chemistry of graphene, Chem. Soc. Rev. 42 (2013) 3222–3233.
[4] V. Georgakilas, M. Otyepka, A.B. Bourlinos, V. Chandra, N. Kim, K.C. Kemp, P. Hobza, R. Zboril, K.S. Kim, Functionalization of graphene: covalent and non-covalent approaches, derivatives and applications, Chem. Rev. 112 (2012) 6156–6214.
[5] H.Y. Mao, Y.H. Lu, J.D. Lin, S. Zhong, A.T.S. Wee, W. Chen, Manipulating the electronic and chemical properties of graphene via molecular functionalization, Prog. Surf. Sci. 88 (2013) 132–159.
[6] H. Lee, K. Paeng, I.S. Kim, A review of doping modulation in graphene, Synth. Met. 244 (2018) 36–47.
[7] G. Wu, X. Tang, M. Meyyappan, K.W.C. Lai, Doping effects of surface functionalization on graphene with aromatic molecule and organic solvents, Appl. Surf. Sci. 425 (2017) 713–721.
[8] M. Bagherzadeh, A. Farahbakhsh, Surface functionalization of graphene, Adv. Mater. (2015) 25–65. Ser.
[9] J.E. Johns, M.C. Hersam, Atomic covalent functionalization of graphene, Accounts Chem. Res. 46 (2013) 77–86.
[10] T. Sainsbury, M. Passarelli, M. Naftaly, S. Gnaniah, S.J. Spencer, A.J. Pollard, Covalent carbene functionalization of graphene: toward chemical band-gap manipulation, ACS Appl. Mater. Interfaces 8 (2016) 4870–4877.
[11] V. Georgakilas, J.N. Tiwari, K.C. Kemp, J.A. Perman, A.B. Bourlinos, K.S. Kim, R. Zboril, Non-covalent functionalization of graphene and graphene oxide for energy materials, biosensing, catalytic and biomedical applications, Chem. Rev. 116 (2016) 5464–5519.
[12] G. Sakellariou, Graphene: from synthesis and functionalization to applications, Curr. Org. Chem. 19 (2015), 1756-1756.
[13] K.R. Nandanapalli, D. Mudusu, S. Lee, Functionalization of graphene layers nd advancements in device applications, Carbon 152 (2019) 954–985.
[14] K.S. Novoselov, Z. Jiang, Y. Zhang, S.V. Morozov, H.L. Stormer, U. Zeitler, J.C. Maan, G.S. Boebinger, P. Kim, A.K. Geim, Room-temperature quantum hall effect in graphene, Science 315 (2007), 1379-1379.
[15] J.R. Williams, L. DiCarlo, C.M. Marcus, Quantum hall effect in a gate-controlled p-n junction of graphene, Science 317 (2007) 638–641.
[16] T. Shen, W. Wu, Q.K. Yu, C.A. Richter, R. Elmquist, D. Newell, Y.P. Chen, Quantum Hall effect on centimeter scale chemical vapor deposited graphene films, Appl. Phys. Lett. 99 (2011).
[17] Y.F. Yang, G.J. Cheng, P. Mende, I.G. Calizo, R.M. Feenstra, C. Chuang, C.W. Liu, C.I. Liu, G.R. Jones, A.R.H. Walker, R.E. Elmquist, Epitaxial graphene homogeneity and quantum Hall effect in millimeter-scale devices, Carbon 115 (2017) 229–236.
[18] Z. Jiang, Y. Zhang, Y.W. Tan, H.L. Stormer, P. Kim, Quantum Hall effect in graphene, Solid State Commun. 143 (2007) 14–19.
[19] J. Jobst, D. Waldmann, F. Speck, R. Hirner, D.K. Maude, T. Seyller, H.B. Weber, Quantum oscillations and quantum Hall effect in epitaxial graphene, Phys. Rev. B (2010) 81.
[20] A. Lartsev, T. Yager, T. Bergsten, A. Tzalenchuk, T.J.B.M. Janssen, R. Yakimova, S. Lara-Alvila, S. Kubatkin, Tunning carrier density across Dirac point in

epitaxial graphene on SC by corona discharge, Appl. Phys. Lett. 105 (2014), 063106.
[21] S.C. Hernandez, D.R. Wheeler, M.S. Osofsky, G.G. Jernigan, V.K. Nagareddy, A. Nath, E.H. Lock, L.O. Nyakiti, R.L. Myers-Ward, K. Sridhara, C.R. Eddy, D.K. Gaskill, S.G. Walton, Plasma-based chemical modification of epitaxial graphene with oxygen functionalities, Surf. Coating. Technol. 241 (2014) 8–12.
[22] R.A. Bueno, J.I. Martinez, R.F. Luccas, N.R. del Arbol, C. Munuera, I. Palacio, F.J. Palomares, K. Lauwaet, S. Thakur, J.M. Baranowski, W. Strupinski, M.F. Lopez, F. Mompean, M. Garcia-Hernandez, J.A. Martin-Gago, Highly selective covalent organic functionalization of epitaxial graphene, Nat. Commun. 8 (2017).
[23] J. Sforzini, P. Hapala, M. Franke, G.v. Straaten, A. Stohr, S. Link, S. Soubatch, P. Jelinek, T.L. Lee, U. Starke, M. Svec, F.C. Bocquet, F.S. Tautz, Structural and electronic properties of nitrogen-doped graphene, Phys. Rev. Lett. 116 (2016) 126805.
[24] H. He, K.H. Kim, A. Danilov, D. Montemurro, L. Yu, Y.W. Park, F. Lombardi, T. Bauch, K. Moth-Poulsen, T. Iakimov, R. Yakimova, P. Malmberg, C. Muller, S. Kubatkin, S. Lara-Avila, Uniform doping of graphene close to the Dirac point by polymer-assisted assembly of molecular dopants, Nat. Commun. 9 (2016) 3956.
[25] A. Rigosi, M. Kruskopf, H.M. Hill, J. Jin, B. Wu, P.E. Johnson, S. Zhag, M. Berilla, A.R.H. Walker, C.A. Hacker, D.B. Newell, R.E. Elmquist, Gateless andreversible carrier density tunability in epitaxial graphene devices functionalized with chromium tricarbonyl, Carbon 142 (2019) 468–474.
[26] M. Baraket, S.G. Walton, E.H. Lock, J.T. Robinson, F.K. Perkins, The functionalization of graphene using electron-beam generated plasmas, Appl. Phys. Lett. 96 (2010) 231501.
[27] M. Yang, O. Couturaud, W. Desrat, C. Consejo, D. Kazazis, R. Yakimova, M. Syvajarvi, M. Goiran, J. Beard, P. Frings, M. Pierre, A. Cresti, W. Escoffier, B. Jouault, Puddle-induced resistance oscillations in the breakdown of the graphene quantum Hall effect, Phys. Rev. Lett. 117 (2016).
[28] E. Pallecchi, M. Ridene, D. Kazazis, C. Mathieu, F. Schopfer, W. Poirier, D. Mailly, A. Ouerghi, Observation of the quantum Hall effect in epitaxial graphene on SiC(0001) with oxygen adsorption, Appl. Phys. Lett. 100 (2012).
[29] B. Jouault, N. Camara, B. Jabakhanji, A. Caboni, C. Consejo, P. Godignon, D.K. Maude, J. Camassel, Quantum Hall effect in bottom-gated epitaxial graphene grown on the C-face of SiC, Appl. Phys. Lett. 100 (2012).
[30] T. Shen, J.J. Gu, M. Xu, Y.Q. Wu, M.L. Bolen, M.A. Capano, L.W. Engel, P.D. Ye, Observation of quantum-Hall effect in gated epitaxial graphene grown on SiC (0001), Appl. Phys. Lett. 95 (2009).
[31] J.A. Alexander-Webber, J. Huang, D.K. Maude, T.J.B.M. Janssen, A. Tzalenchuk, V. Antonov, T. Yager, S. Lara-Avila, S. Kubatkin, R. Yakimova, R.J. Nicholas, Giant quantum Hall plateaus generated by charge transfer in epitaxial graphene, Sci. Rep. UK 6 (2016) 1–11.
[32] S. Lara-Avila, K. Moth-Poulsen, R. Yakimova, T. Bjornholm, Y. Falko, A. Tzalenchuk, S. Kubatkin, Non-volatile photochemical gating of an epitaxial graphene/polymer heterostructure, Adv. Mater. 23 (2011) 878–882.
[33] E.H. Lock, M. Baraket, M. Laskoski, S.P. Mulvaney, W.K. Lee, P.E. Sheehan, D.R. Hines, J.T. Robinson, J. Tosado, M.S. Fuhrer, S.C. Hernandez, S.G. Walton, High-quality uniform dry transfer of graphene to polymers, Nano Lett. 12 (2012) 102–107.
[34] E.H. Lock, D.M. Delongchamp, S.W. Schmucker, B. Simpkins, M. Laskoski, S.P. Mulvaney, D.R. Hines, M. Baraket, S.C. Hernandez, J.T. Robinson, P.E. Sheehan, C. Jaye, D.A. Fisher, S.G. Walton, Dry graphene transfer print to polystyrene and ultra-high molecular weight polyethylene - detailed chemical, structural, morphological and electrical characterization, Carbon 86 (2015) 288–300.
[35] H. Liu, Y. Liu, D. Zhu, Chemical doping of graphene, J. Mater. Chem. 21 (2011) 3335–3345.
[36] D.B. Farmer, V. Perebeinos, Y.-M. Lin, C. Dimitrakopoulos, P. Avouris, Charge trapping and scattering in epitaxial graphene, Phys. Rev. B 84 (2011) 205417.
[37] S. Kopylov, A. Tzalenchuk, S. Kubatkin, V. Fal'ko, Charge transfer between epitaxial graphene and silicon carbide, Appl. Phys. Lett. 97 (2010) 112109.
[38] F. Giannazzo, I. Deretzis, A. La Magna, F. Roccaforte, R. Yakimova, Electronic transport at monolayer-bilayer junctions in epitaxial graphene on SiC, Phys. Rev. B 86 (2012) 235422.
[39] T. Schumann, K.J. Friedland, M.H. Oliveira, A. Tahraoui, J.M.J. Lopes, H. Riechert, Anisotropic quantum Hall effect in epitaxial graphene on stepped SiC surfaces, Phys. Rev. B 85 (2012) 235402, 85 (2012).
[40] Y. Matsubara, K.S. Takahashi, M.S. Bahramy, Y. Kozuka, D. Maryenko, J. Falson, A. Tsukazaki, Y. Tokura, M. Kawasaki, Observation of the quantum Hall effect in delta-doped SrTiO3, Nat. Commun. 7 (2016) 11631.
[41] R. Akiyama, Y. Takano, Y. Endo, S. Ichinokura, R. Nakanishi, K. Nomura, S. Hesegawa, Berry phase shift from 2pi to pi in bilayer graphene by Li-intercalation and sequential desorption, Appl. Phys. Lett. 110 (2017) 233106.
[42] K.S. Novoselov, A.K. Geim, S.V. Morozov, D. Jiang, M.I. Katsnelson, I.V. Grigorieva, S.V. Dubonos, A.A. Firsov, Two-dimensional gas of massless Dirac fermions in graphene, Nature 438 (2005) 197–200.
[43] P. Giannozzi, S. Baroni, N. Bonini, M. Galandra, R. car, C. Cavazzoni, D. Ceresoli, G.L. Chiarotti, M. Cococcioni, I. Dabo, A.D. Corso, S.d. Gironcoli, S. Fabris, G. Fratesi, R. Gebauer, U. Gerstmann, C. Gougoussis, A. Kokalj, M. Lazzeri, L. Martin-Samos, N. Marzari, F. Mauri, R. Mozzarello, S. Paolini, A. Rasquarello, L. Paulatto, C. Sbraccia, S. Scandolo, G. Schauzero, A.P. Seitsonen, A. Smogunov, P. Umari, R.M. Wetzcovitch, Quantum Espresso: a modular and open-source software project for quantum simulation of materials, J. Phys. Condens. Matter 21 (2009) 395502–395521.
[44] J.P. Perdew, Y. Wang, Phys. Rev. B 33 (1986) 8800.
[45] J.P. Perdew, K. Burke, M. Ernzerhof, Generalized gradient approximation made simple, Phys. Rev. Lett. 77 (1996) 3865–3868.
[46] S. Grimme, Semiempirical GGA-type density function; constructed with a long-range dispersion correction, J. Comput. Chem. 27 (2006), 1887-1799.
[47] V. Barone, M. Casarin, D. Forrer, M. Pavone, M. Sambi, A. Vittadini, Role and effective treatment of dispersive forces in materials: polyethylene and graphite crystals as test cases, J. Comput. Chem. 30 (2008) 934–939.
[48] K.M. Daniels, M.M. Jadidi, A.B. Sushkov, A. Nath, A.K. Boyd, A. Sridhara, H.D. Drew, T.E. Murphy, R.L. Myers-Ward, D.K. Gaskill, Narrow plasmon resonances enabled by quasi-freestanding bilayer epitaxial graphene, 2D Mater. 4 (2017), 025034.
[49] H.J. Monkhorst, J.D. Pack, Special points for Brillouin-zone integrations, Phys. Rev. B 13 (1976) 5188–5192.
[50] A. Nath, A.D. Koehler, G.G. Jernigan, V.D. Wheeler, J.K. Hite, S.C. Hernandez, Z.R. Robinson, N.Y. Garces, R.L. Myers-Ward, C.R. Eddy, D.K. Gaskill, M.V. Rao, Achieving clean epitaxial graphene surfaces suitable for device applications by improved lithographic process, Appl. Phys. Lett. 104 (2014).
[51] A. Nath, B.D. Kong, A.D. Koehler, V.R. Anderson, V.D. Wheeler, K.M. Daniels, A.K. Boyd, E.R. Cleveland, R.L. Myers-Ward, D.K. Gaskill, K.D. Hobart, F.J. Kub, G.G. Jernigan, Universal conformal ultrathin dielectrics on epitaxial graphene enabled by a graphene oxide seed layer, Appl. Phys. Lett. 110 (2017).